RSC Advances

PAPER

View Article Online
View Journal | View Issue

Open Access Article. Published on 07 September 2020. Downloaded on 1/24/2025 5:26:30 AM.
This article is licensed under a Creative Commons Attribution-NonCommercial 3.0 Unported Licence.

Check for updates

Cite this: *RSC Adv.*, 2020, **10**, 33059

Dry reforming of methane over nickel supported on Nd–ceria: enhancement of the catalytic properties and coke resistance†

Hugo A. Lara-García,* Daniel G. Araiza, Melissa Méndez-Galván, Samuel Tehuacanero-Cuapa, Antonio Gómez-Cortés and Gabriela Díaz*

Received 1st July 2020
Accepted 28th August 2020

DOI: 10.1039/d0ra05761d

rsc.li/rsc-advances

Nickel (5 wt%) supported on Nd-doped ceria was studied as catalysts in the DRM reaction at stoichiometric conditions in the range of 600–800 °C. $Ce_{1-x}Nd_xO_{2-\delta}$ supports with different Nd contents ($x = 0$, 0.05, 0.1 and 0.2) were successfully synthesized. The role of oxygen vacancies by the incorporation of Nd^{3+} into the ceria lattice was investigated. These species were quantified by XRD and Raman spectroscopy, showing a linear dependence as a function of Nd content. Ni/Nd–ceria catalysts were prepared by wet impregnation. Although formation of oxygen vacancies, as well as microstructural features of the support (smaller crystallite sizes, higher surface area, and developed mesoporous structure) were improved as a function of the Nd content, no significant differences were observed in the catalytic properties of Ni/Nd–ceria in the DRM reaction. Despite this, compared to undoped ceria, all the Nd-doped CeO_2 catalysts present an enhanced activity and stability, and the best catalytic performance was observed in the $Ni/Ce_{0.95}Nd_{0.05}O_{2-\delta}$ sample. Quantification of carbon residues in spent catalysts showed, as expected, lower amounts in the Ni/Nd–ceria samples; nevertheless, among them, the catalyst with the higher amount of oxygen vacancies, is the one with the higher carbon residues. Incorporation of Nd in ceria changes the acid/base properties, diminishing the gasification capacity of the carbonaceous species. These results emphasize that the activity and stability in the Ni/Nd–ceria catalysts for the DRM reaction depend on two key factors, the redox and the acid/base properties of the CeO_2 supports, offering insights about the necessary and adequate balance between these properties.

1. Introduction

The dry reforming of methane (DRM) reaction, eqn (1), is a catalytic route suitable for diminishing two abundant atmospheric pollutants, carbon dioxide, and methane.[1] The reaction products, hydrogen, and carbon monoxide (a mixture known as synthesis gas) are the base for producing a great variety of high-value chemicals.[2] Overall, the DRM reaction is a sustainable process that removes contaminants from the environment while producing important compounds; thus, the investigation related to the design of stable catalysts operating at high temperature in the DRM reaction (due to its endothermicity), eqn (1) has grown in the last years.[3]

$$CH_4 + CO_2 \leftrightarrow 2H_2 + 2CO, \quad \Delta H = +247.3 \text{ kJ mol}^{-1} \qquad (1)$$

Nickel-based catalysts have been widely employed in the DRM reaction, owing to their high activity, considerable availability and low cost.[4] The main drawback of Ni in reforming reactions is its tendency to promote the formation of carbon deposits, which deactivate the catalyst;[5] this behavior becomes more relevant when catalysts are submitted to high-temperature regimes, as in the case of the DRM reaction.

A strategy to mitigate the formation of carbon deposits over the surface of catalysts has been the use of "non-innocent" supports like CeO_2 or La_2O_3 whose surface chemistry/reducibility is very rich, promoting the gasification of carbon species.[6] In this sense, the use of nickel–ceria catalysts in the DRM reaction combines the high intrinsic activity of the Ni active phase with the redox surface properties of CeO_2 support (Ce^{4+}/Ce^{3+}); vast literature concerning this system has been published.[7–10]

In a continuous search for the further improvement of catalytic properties of the Ni/CeO_2 system in the DRM reaction, different routes can be explored, as addition of a second metal[11] or modification of the support.[12] The former was already investigated by our group, where we found that small additions of Pt to nickel–ceria catalysts, considerably boost the catalytic properties in the DRM reaction.[13]

By focusing on the modification of ceria, different strategies have been reported to positively impact the properties,

Instituto de Física, Universidad Nacional Autónoma de México, Apartado Postal 20364, CDMX 01000, Mexico. E-mail: hugo.lara@fisica.unam.mx; diaz@fisica.unam.mx

† Electronic supplementary information (ESI) available. See DOI: 10.1039/d0ra05761d

Open Access Article. Published on 07 September 2020. Downloaded on 1/24/2025 5:26:30 AM.
This article is licensed under a Creative Commons Attribution-NonCommercial 3.0 Unported Licence.

especially on the oxygen storage capacity.[14] Doping the structure with an additional component results in the generation of a substitutional solid solution, $Ce_{(1-x)}M_xO_{2-\delta}$, where an oxygen vacancy is created in order to fulfill charge neutrality.[15] Doping CeO_2 with trivalent rare-earth elements as neodymium (Nd), samarium (Sm) and gadolinium (Gd), among others, has resulted effective in the generation of oxygen vacancies and surface defects.[16–18] Compared to other lanthanides, Nd presents a high solubility in CeO_2, along with an enhanced oxygen diffusion coefficient, features which promote the formation of a solid solution and generation of oxygen vacancies.[19–21] Among the different routes to prepare doped ceria powders, EDTA–citrate complexing synthesis method is a simple route to obtain different compositions of rare earth doped-ceria, and the process inhibits crystalline growth and grain growth.[22]

In the specialized literature, very few examples of the use of Nd_2O_3 mainly as promoter for Ni-based catalysts can be found; the addition of Nd oxide favored interactions between Ni and supports (SBA-15 and Mg–Al–O) enhancing the catalytic performance.[23,24] However, to the best of our knowledge, catalysts composed of nickel supported over Nd-doped ceria with variable composition have not been tested in the DRM reaction; thus this strategy to improve the catalytic properties of nickel–ceria catalysts is completely new and results will contribute to the use of new and efficient catalysts in this on-growing field.

In this frame, this work aimed to study the influence of Nd-doped CeO_2 in the catalytic properties of Ni/CeO_2 for dry reforming of methane. Results showed that Nd incorporation develops a mesoporous structure in the support, higher specific surface area, lower crystallite size, and increased number of oxygen vacancies as a function of the dopant content. Ni/Nd–ceria catalysts are more active and stable in DRM reaction than Ni/CeO_2. Despite the microstructural properties and the enhanced oxygen vacancies, carbon deposition on Ni/Nd–ceria catalysts increases as a function of Nd concentration in the support. An adequate balance between redox and acid/base properties directly related to the Nd concentration is needed to fully develop the enhanced catalytic properties of Ni/Nd–ceria catalysts.

2. Experimental section

2.1 Synthesis of materials

2.1.1 Ceria and Nd-doped ceria supports *via* EDTA–citrate complexing method. $Ce_{1-x}Nd_xO_{2-\delta}$ (x = 0, 0.05, 0.1 and 0.2) were synthesized by the combined EDTA–citrate complexing method.[22] Firstly, stoichiometric amounts of the corresponding metal nitrates ($Ce(NO_3)_3 \cdot 6H_2O$, 99.0% Sigma-Aldrich and $Nd(NO_3)_3 \cdot 6H_2O$, 99.9% Sigma-Aldrich) were dissolved in deionized water. The solution was heated to 70 °C and stirred during 1 h. Anhydrous citric acid ($C_6H_8O_7$ 99.98%, Sigma-Aldrich) and EDTA ($C_{10}H_{16}N_2O_8$ 98.5%, Sigma-Aldrich) were separately dissolved in an ammonium hydroxide dissolution (NH_4OH 28–30%, Sigma-Aldrich), controlling the pH value at around 7. Then, these two solutions were heated to 90 °C under stirring and subsequently dropped simultaneously to the aqueous metal nitrates-containing solution. The pH of the resultant solution was monitored and keep at around 7 by dropping an excess of aqueous ammonia solution. The molar ratio was 1 : 1 : 1 for metal cations : citric acid : EDTA. A transparent solution was obtained and subsequently heated to 90 °C, while it was stirred. After water evaporation, a viscous gel was obtained. Then the gel was combusted at about 300 °C to remove the organic matter. The resultant yellow powder was calcined at 500 °C for 8 h under air atmosphere.

2.1.2 Ni supported on ceria catalysts. Synthesis of nickel catalysts supported on pristine ceria and Nd-doped ceria was achieved by wet impregnation, with total metal content of 5 wt%. Appropriate amounts of $Ni(NO_3)_2 \cdot 6H_2O$ (99.98%, Aldrich) were dissolved in deionized water and added dropwise to the stirring support suspension. After 0.5 h of mixture at room temperature, the solvent was slowly evaporated by placing the flask in a controlled bath at 65 °C. Finally, materials were calcined at 600 °C (10 °C min^{-1}) for 4 h in air flow (30 mL min^{-1}).[25]

2.2 Characterization of materials

X-ray diffraction (XRD) was employed to elucidate the crystalline phases and the effect of the Nd into the crystalline structure of the support and catalysts. Analysis were performed at room temperature in a Bruker D8 diffractometer with CuKα radiation (λ = 0.154 nm) equipped with a Ni-0.5% Cu-Kα filter in the secondary beam, and a one-dimensional position-sensitive silicon strip detector (Bruker, Lynxeye). The diffraction intensity as a function of 2θ angles was measured between 10° and 80°, with a 2θ step of 0.021° and 144 s per point. In order to determine the average crystal size and the lattice parameter of materials, Rietveld refinement of the XRD data was performed by using the BGMN program and the graphical interface Profex.[26] Structure of the materials was also analyzed by Raman spectroscopy using a Thermo Scientific DRX Raman Microscope with and excitation wavelength of 532 nm (10 mW) and a spectral resolution of 2 cm^{-1}. All Raman spectra were recorded at ambient conditions.

Textural properties of catalysts were determined by N_2 adsorption at −196 °C in a Quantachrome Autosorb MP-1 equipment. The materials (0.050 g) were degasified under vacuum at 200 °C for 4 h before each analysis. The BET and BJH methods were used for calculation of the specific surface area and the pore size distribution, respectively.

Microstructure of the samples was studied by scanning electron microscopy (SEM). Backscattering electron images were obtained using a JEOL JMS-7800F Schottky Field Emission Scanning Electron Microscope. For the analysis, the samples were deposited on holey carbon coated copper grids. Estimation of the metal content was carried out by energy-dispersive X-ray spectroscopy (EDS) analysis. Powders were dispersed onto carbon-supported aluminum holders and measurements were performed using a Thermo Noran microanalysis system coupled to a SEM JEOL 5600, working at 20 kV and using a magnification of 500×. Resulting spectra were compared with data collected from standards stored in the system library, *i.e.*, through a semi-quantitative analysis approach.

Reduction properties of the catalyst were studied through hydrogen temperature programmed reduction experiments (H_2-

Open Access Article. Published on 07 September 2020. Downloaded on 1/24/2025 5:26:30 AM.
This article is licensed under a Creative Commons Attribution-NonCommercial 3.0 Unported Licence.

TPR) in an ISRI RIG-100 multitask apparatus equipped with a fixed-bed quartz reactor and a thermal conductivity detector (TCD). Materials (0.050 g) were pre-treated *in situ* in air atmosphere (30 mL min^{-1}) at 300 °C for 1 h and cooled in N_2 flow (30 mL min^{-1}) down to room temperature, prior to experiments. Reduction was performed using a 5% H_2/N_2 gas mixture flow (30 mL min^{-1}) from room temperature up to 800 °C, with a heating rate of 10 °C min^{-1}. The H_2O produced by the reduction process was trapped before entered the TCD.

Temperature programmed oxidation of spent catalysts after stability tests (700 °C/24 h) were studied through O_2-TPO experiments in order to elucidate the type and quantity of carbon deposits on the surface of the catalysts. In a typical procedure, an amount of the spent catalyst (0.050 g) is transferred to a fixed-bed quartz reactor placed in a home-made dynamic reaction system coupled to a HIDEN HPR20 QMS. The sample is treated with argon flow (30 mL min^{-1}) at 100 °C for 1 h before running the experiments to remove residual adsorbed species from the catalyst surface. Oxidation takes place by admission of a gas mixture flow of 20% O_2/He (30 mL min^{-1}) in the range of 100–800 °C at a heating rate of 10 °C min^{-1}. Production of CO_2 was monitored following the $m/z = 44$ value.

2.3 Catalytic tests

The dry reforming of methane reaction was performed using a fixed-bed quartz reactor under atmospheric pressure and continuous flow of reactants. All activity tests were carried out with the same amount of sample (0.100 g) in the 600–800 °C temperature range and data acquisition every 50 °C, in a steady state regime. On the other side, stability tests were done also with a fixed amount of catalyst (0.100 g) at constant temperature (700 °C) for 24 h, and collecting data each 0.5 h. Prior to experiments, catalysts were *in situ* reduced with a flow of 10% H_2/N_2 (60 mL min^{-1}) at 600 °C (10 °C min^{-1}) for 2 h. Afterwards, catalysts were purged in argon atmosphere (60 mL min^{-1}) and temperature was set to the initial value, depending on the catalytic test. The reactant mixture with molar ratio $CH_4 : CO_2 = 1 : 1$ (40 vol% of each compound and argon balance, total flow = 100 mL min^{-1}) was fed into the system at a GHSV = 48 000 h^{-1}. Products were analyzed by gas chromatography using a GOW-MAC apparatus with a TCD detector and a Carbosphere packed column.

The conversion of methane (CH_4 (%)) and carbon dioxide (CO_2 (%)) along with the H_2/CO molar ratio ($Y_{H_2/CO}$) were calculated as follows:

$$CH_4\ (\%) = \{[CH_4(in) - CH_4(out)]/CH_4(in)\} \times 100$$

$$CO_2\ (\%) = \{[CO_2(in) - CO_2(out)]/CO_2(in)\} \times 100$$

$$Y_{H_2/CO} = H_2(out)/CO(out)$$

where: CH_4(in) and CO_2(in) are the mole of methane and carbon dioxide admitted in the reactor; CH_4(out) and CO_2(out) are the mole of methane and carbon dioxide measured in the effluent; H_2(out) and CO(out) are the mole of hydrogen and carbon monoxide produced in the reaction.

3. Results and discussion

3.1 Nd–CeO_2 supports

3.1.1 X-ray diffraction analysis. Pristine CeO_2 and Nd-doped ceria supports were synthesized by EDTA–citrate complexing method with different loadings of neodymium: 0, 5, 10 and 20 at%. Fig. 1 shows the XRD patterns of the as-prepared samples. In all cases, the diffraction peaks depicted are related to the fluorite cubic structure of CeO_2 (JCPDS 034-0394), and no other contributions are observed. The absence of other peaks indicates in a first approximation proper incorporation of Nd into CeO_2 crystal structure. It is evident (Fig. 1 inset) that the diffraction peaks are shifted to lower angles as a function of the Nd content, which means a lattice expansion. The lattice parameter and crystal size were obtained by Rietveld refinement, and results are presented in Table 1. Lattice parameter values increase as a function of Nd content, from 5.4115 Å in pure ceria to 5.4479 Å when 20 at% of Nd was introduced. This result is in good agreement considering the ionic radii of Ce^{4+} and Nd^{3+}, 0.97 and 1.11 Å, respectively. The trivalent neodymium ions replace the Ce^{4+} ions in the lattice, generating oxygen vacancies to maintain the charge neutrality. The formation of oxygen vacancies can be written using the Kröger–Vink notation as follows:

$$2CeO_2 \xrightarrow{Nd_2O_3} 2Nd'_{Ce} + 3O_o^{\times} + V_o^{\cdot\cdot} + \frac{1}{2}O_2 \quad (2)$$

where $O_o^{\times}$ denotes the O ion occupying the oxygen lattice, $2Nd'_{Ce}$ denotes the Nd ion occupying the Ce lattice with a negative single charge, and $V_o^{\cdot\cdot}$ denotes an oxygen vacancy with a doubly positive charge. Additionally, crystallite size decreases as a function of the Nd content from 19.24 to 12.01 nm. This was previously observed in La-doped ceria, where by increasing the dopant concentration from 0.05 to 0.4, the crystallite size was found to enhance the oxygen defects (Ce^{3+} sites) in ceria.[27] Therefore, in addition to the dopant mediated oxygen vacancies formation, the crystallite size also generates oxygen vacancies.

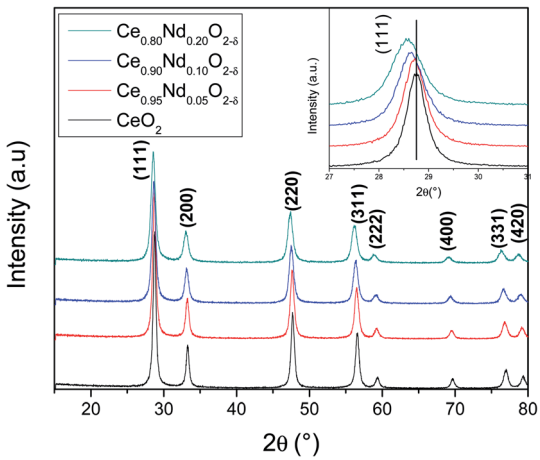

Fig. 1 XRD patterns of as-prepared CeO_2 and Nd-doped ceria supports. Inset displays a diffraction peak zoom of principal reflection of ceria.

Open Access Article. Published on 07 September 2020. Downloaded on 1/24/2025 5:26:30 AM.
This article is licensed under a Creative Commons Attribution-NonCommercial 3.0 Unported Licence.

Table 1 Lattice parameter, and average crystal size calculated considering (111) plane of CeO_2 and Nd-doped ceria supports

Support	Lattice parameter a_0 (Å)	Crystallite size (111) (nm)
CeO_2	5.4115	19.24
$Ce_{0.95}Nd_{0.05}O_{2-\delta}$	5.4204	16.25
$Ce_{0.9}Nd_{0.1}O_{2-\delta}$	5.4304	14.03
$Ce_{0.8}Nd_{0.2}O_{2-\delta}$	5.4479	12.01

3.1.2 Raman spectroscopy and oxygen vacancies. To further analyze the oxygen defects created by the introduction of Nd into the ceria structure, Raman spectroscopy experiments were carried out. Fig. 2 shows Raman spectra of as-prepared supports. The spectrum of pristine ceria presents a single sharp band at 472 cm^{-1}, the characteristic F_{2g} peak attributed to the vibrational mode of oxygen atoms surrounding cerium in the fluorite crystal structure.[28] This band is also observed in the Nd-doped ceria spectra, shifted to lower wavenumbers. Additionally, two other peaks are observed at 558 cm^{-1} (α) and 611 cm^{-1} (β) in the Nd-doped samples; the bands intensity increases as a function of Nd content. It has been reported that these bands are related to oxygen vacancies and/or structural defects generated by the incorporation of rare-earth ions into the ceria crystal structure.[29,30] The α peak is commonly known as extrinsic oxygen vacancies and is associated to oxygen vacancies produced in order to maintain the charge neutrality when Ce^{4+} ions are substituted by Nd^{3+} ions. On the other hand, the β band (intrinsic oxygen vacancies) is attributed to oxygen vacancies that are generated by the presence of Ce^{3+} ions. The intensity of these bands is related to the number of oxygen vacancies and the increment in the intensities as a function of Nd content is indicative of the well incorporation of Nd into CeO_2 crystal structure, which is in a good agreement with XRD results. Moreover, in a previous report it was demonstrated that the solubility limit of Nd into the CeO_2 crystal structure is 40 at%.[20]

Additionally, oxygen vacancies can be calculated by correlating the shift in the main F_{2g} band.[28,31] For pristine ceria this value is estimated by $\Delta\omega = -\gamma\omega/(\Delta V/V_0)$, where ω is the shift in Raman frequency, γ is the Grüneisen parameter (1.24 for this mode), and ΔV is the volume change from the reference volume. Volume changes of the unit cell are due to expansion of Ce^{4+} to Ce^{3+} (ionic radii 0.97 Å and 1.14 Å, respectively), which is only partially counterbalance by the compression due to loss of O^{2-} (ionic radius 1.380 Å) leading to oxygen vacancies (1.164 Å). The relationship between the oxygen vacancy concentration δ and the change in volume $\Delta V/V_0$ is linear: $\delta = -10(\Delta a/a_0) = -3.3(\Delta V/V_0)$, where $(\Delta a/a_0)$ is the change in the lattice constant. For pristine ceria, the oxygen deficit is then:

$$\delta = 2.66(\Delta\omega/\omega_0) \quad (3)$$

In the present investigation, the change in the volume is not only caused by cerium ions, but there is an additional contribution by neodymium incorporation. Nevertheless, the Nd^{3+} ionic radius is like the Ce^{3+} ionic radius, 1.11 and 1.14 Å, respectively. Therefore, using eqn (3) and taking as reference the pristine ceria Raman spectrum (assuming no oxygen vacancies in pure ceria) lead us to have a good approximation of the oxygen vacancies generated by the incorporation of Nd into the fluorite ceria crystal structure.

Table 2 shows the oxygen vacancies calculated by Raman spectroscopy using eqn (2) and by Rietveld refinement, using the $\delta = -10(\Delta a/a_0)$ equation, and taking as a reference the pristine ceria lattice parameter (a_0). It is evident that oxygen vacancies increase linearly as a function of neodymium content when calculated by Raman spectroscopy; this result was expected as the magnitude of the downshift of the F_{2g} Raman mode varies well linearly as a function of Nd. On the other hand, oxygen vacancies calculated by the lattice parameter change almost linearly. These results confirm the formation of oxygen vacancies by the good incorporation of Nd into the ceria crystal structure. Oxygen vacancies are related to the enhancement of the catalytic behavior as is shown ahead.

3.1.3 Textural properties and metal content. The supports were characterized by N_2 adsorption–desorption. Fig. 3(a) shows the nitrogen adsorption–desorption isotherms. Pristine CeO_2 presents a type II isotherm with a negligible hysteresis loop; according to the IUPAC, this isotherm type is related to non-porous or macroporous materials.[32] On the contrary, all Nd-doped ceria supports present a type IV isotherm with hysteresis loop type H1 suggesting mesoporous materials.[33] The pore-size distribution curves of as-prepared supports based on the

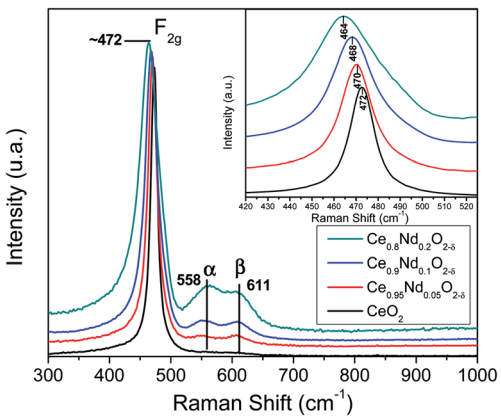

Fig. 2 Raman spectra of as-prepared supports. Inset displays the Raman shift in the F_{2g} Raman band.

Table 2 Oxygen vacancies calculated by Raman spectroscopy and XRD results

Support	Raman shift F_{2g} (cm^{-1})	Oxygen vacancies Raman	Lattice parameter a_0 (Å)	Oxygen vacancies XRD
CeO_2	472	0	5.4115	0
$Ce_{0.95}Nd_{0.05}O_{2-\delta}$	470	0.011	5.4204	0.0089
$Ce_{0.9}Nd_{0.1}O_{2-\delta}$	468	0.022	5.4304	0.0189
$Ce_{0.8}Nd_{0.2}O_{2-\delta}$	464	0.044	5.4479	0.0364

Open Access Article. Published on 07 September 2020. Downloaded on 1/24/2025 5:26:30 AM.
This article is licensed under a Creative Commons Attribution-NonCommercial 3.0 Unported Licence.

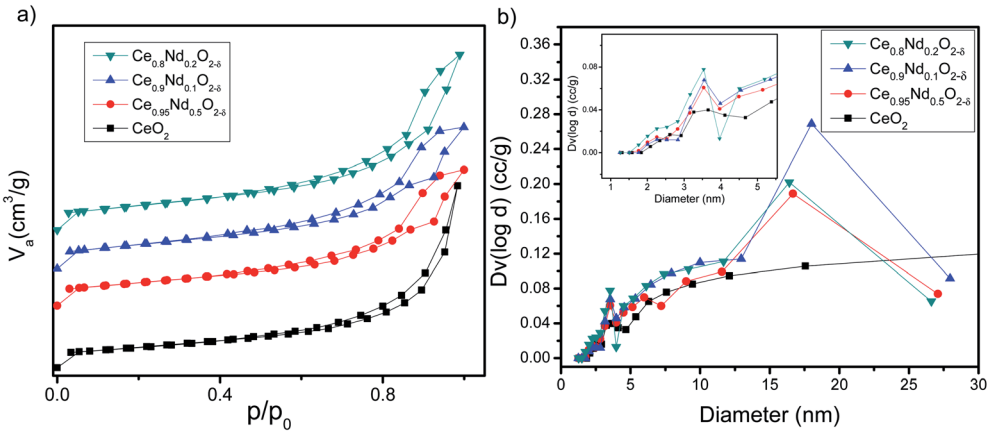

Fig. 3 (a) N_2 adsorption–desorption isotherms and (b) BJH pore size distribution of as-prepared supports. Inset displays BJH pore sizes distributions between 0 and 5 nm.

Barrett–Joyner–Halenda (BJH) method are presented in Fig. 3(b).

It is clear that Nd-doped ceria shows a hierarchically bi-modal porous structure with an apex at 3.5 nm (Fig. 3(b) inset) and the other one between 16 and 18 nm, both fall in the mesoporous range; while pristine ceria only presents the first one as a small maximum. It has been demonstrated that the presence of bi-modal porous architecture has a positive effect on the enhancement of catalytic activity because the interconnected internal void space could act as effective transport pathways.[33,34] Additionally, the specific surface area (SSA) was calculated using the BET model and results are shown in Table 3. All the supports present an area around 40 m^2 g^{-1}; nevertheless, there is a slight increment as a function of Nd content; pristine ceria exhibits 37 m^2 g^{-1}, while $Ce_{0.8}Nd_{0.2}O_{2-\delta}$, 43 m^2 g^{-1}. The total pore volume follows the same trend. Finally, as-prepared supports were characterized through EDS analysis to assess the total neodymium content as an atomic percentage; results are presented in Table 3. The Nd contents are 4.8, 9.3, and 20.0 at% for the nominal 5, 10, and 20 at%, respectively.

Additionally, the microstructure of the supports was studied by SEM. Fig. 4 shows the backscattering SEM images of: (a) CeO_2, (b) $Ce_{0.95}Nd_{0.05}O_{2-\delta}$, (c) $Ce_{0.9}Nd_{0.1}O_{2-\delta}$, and (d) $Ce_{0.8}Nd_{0.2}O_{2-\delta}$. The principal difference between pristine ceria and Nd-doped ceria is the development of porosity as a function of the Nd content. This observation is in good agreement with the N_2 adsorption–desorption results, where the total pore volume increases as the Nd content, impacting in the specific surface area.

3.1.4 Reduction properties of Nd–CeO_2 supports. H_2-TPR profiles of supports are presented in Fig. 5. According to the literature, ceria presents two reduction peaks at around 550 and 850 °C that correspond to surface and bulk reduction, respectively.[25] As observed, all samples present the surface reduction peak at around 550 °C, and as the experiments were carried out only up to 800 °C, the bulk reduction peak is not entirely depicted and only the beginning of the hydrogen uptake is observed at 700 °C. The surface reduction peak in all the Nd–ceria samples shifts to higher temperature; for pristine ceria the peak is located at 530 °C while in Nd-doped samples it appears between 545 and 560 °C. The peak area increases as a function of neodymium content, revealing that the addition of neodymium has an impact on the abundance of surface lattice oxygen. On the other hand, it seems that the bulk reduction peak of ceria in the $Ce_{0.8}Nd_{0.2}O_{2-\delta}$ support has shifted to lower temperatures, as a maximum is observed below 700 °C, while in the others, this takes place at higher temperatures as in pure ceria. It has been reported that doping ceria with rare-earth cations has an impact in the bulk reduction properties, shifting the bulk reduction peak to lower temperatures.[35,36] In $Ce_{0.75}RE_{0.25}O_{2-\delta}$ samples doped with 25 at% (RE = Sm, Gd and Nd), it was difficult to distinguish between surface and bulk reduction, as both reduction peaks appear together.[30]

Table 3 Textural properties and neodymium content of as-prepared supports

Support	Specific surface area (m^2 g^{-1})	BJH pore diameter (nm)	Pore volume (cm^3 g^{-1})	Nd content[a] (at%)
CeO_2	37	—	0.103	0
$Ce_{0.95}Nd_{0.05}O_{2-\delta}$	40	3.5 and 16	0.137	4.8
$Ce_{0.9}Nd_{0.1}O_{2-\delta}$	42	3.5 and 18	0.139	9.3
$Ce_{0.8}Nd_{0.2}O_{2-\delta}$	43	3.5 and 16	0.144	20.0

[a] Determined by EDS.

Open Access Article. Published on 07 September 2020. Downloaded on 1/24/2025 5:26:30 AM.
This article is licensed under a Creative Commons Attribution-NonCommercial 3.0 Unported Licence.

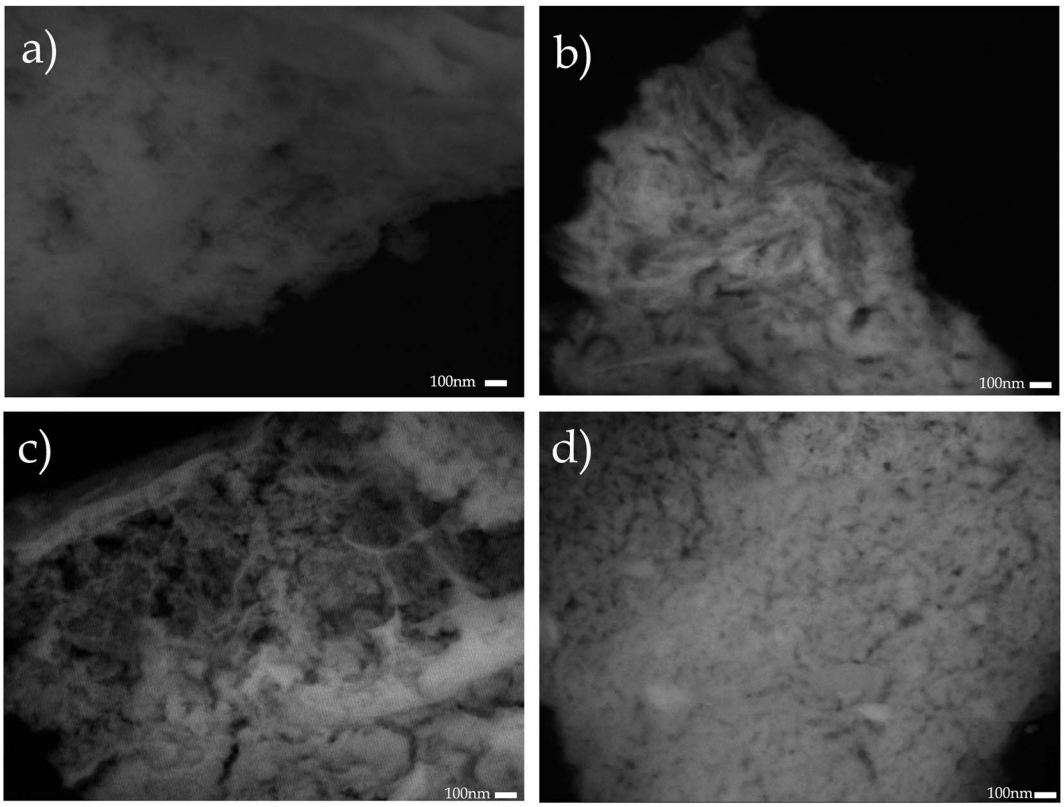

Fig. 4 Backscattering SEM images of the Nd-doped supports: (a) CeO_2, (b) $Ce_{0.95}Nd_{0.05}O_{2-\delta}$, (c) $Ce_{0.9}Nd_{0.1}O_{2-\delta}$, and (d) $Ce_{0.8}Nd_{0.2}O_{2-\delta}$.

3.2 Ni/Nd–CeO_2 catalysts

3.2.1 X-ray diffraction analysis. As-prepared supports were impregnated with nickel with a nominal loading of 5 wt% in all the cases. Structural characterization was carried out by X-ray diffraction. Fig. 6 shows the XRD patterns where the ceria fluorite structure is preserved. Additionally, three new low-intensity diffraction peaks (Fig. 6, inset) depicted at 2θ angles of 37, 43, and 63° are associated to the NiO phase (JCPDS 44-1159). Rietveld refinement of the XRD patterns was carried out, and results are shown in Table 4. Results show that the lattice parameters and the crystallite size of all the supports do not change significantly after nickel impregnation, however some trends are observed, mostly an increase in the former.

3.2.2 Textural properties and metal content. The textural properties of as-prepared catalysts were evaluated by N_2 adsorption–desorption experiments. Fig. 7(a) shows the

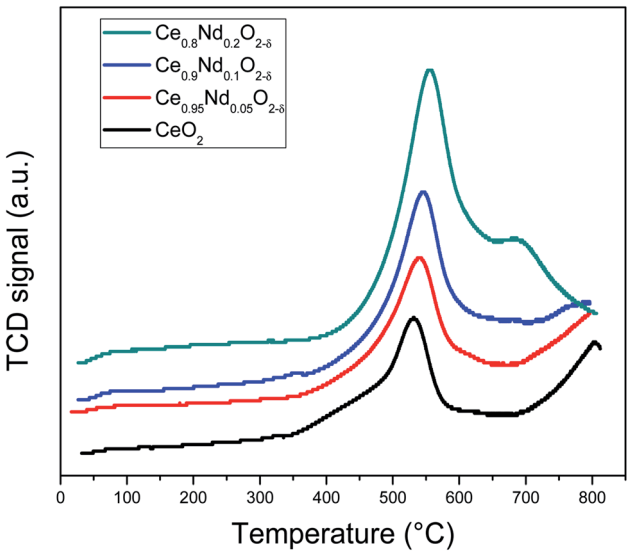

Fig. 5 H_2-TPR profiles of as-prepared CeO_2 and Nd-doped ceria supports.

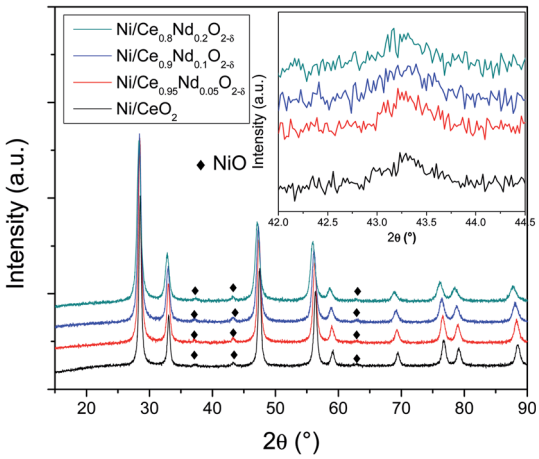

Fig. 6 XRD patterns of as-prepared Ni/CeO_2 and Ni/Nd–ceria catalysts. Inset displays an amplification where the principal diffraction peak of NiO phase resides.

Open Access Article. Published on 07 September 2020. Downloaded on 1/24/2025 5:26:30 AM.
This article is licensed under a Creative Commons Attribution-NonCommercial 3.0 Unported Licence.

Table 4 Ni/CeO_2 and Ni/Nd–ceria catalysts characterization. Lattice parameter, average crystallite size determined considering (111) plane, S_{BET}, and nickel content

Catalyst	Lattice parameter[a] a_0 (Å)	Crystallite size[a] (111) (nm)	Specific surface area ($m^2\ g^{-1}$)	Pore volume ($cm^3 g^{-1}$)	Ni content[b] (wt%)
Ni/CeO_2	5.4119	18.77	33	0.059	4.7
Ni/$Ce_{0.95}Nd_{0.05}O_{2-\delta}$	5.4212	16.22	37	0.069	4.5
Ni/$Ce_{0.9}Nd_{0.1}O_{2-\delta}$	5.4312	14.04	40	0.070	4.8
Ni/$Ce_{0.8}Nd_{0.2}O_{2-\delta}$	5.4490	12.28	41	0.076	4.8

[a] Calculated by Rietveld refinement. [b] Determined by EDS.

adsorption isotherms, noticing that all the catalysts present a type II isotherm as the undoped support, which is related to non-porous or macroporous materials. The pore size distribution in nickel-supported catalysts (Fig. 7(b)) does not present an apparent hierarchal behavior as observed before in Nd-doped ceria supports. The specific surface area (SSA) results are shown in Table 4. The SSA of the catalysts slightly decreases compared to the doped supports (Table 3), but almost a two-fold decrease in the total pore volume is observed. The reduction in the SSA after impregnation with nickel is related to occlusion of pores by nickel particles affecting the original mesoporous structure of the supports. This behavior is in good agreement with previous reports.[37–39] Despite this, the general trend is maintained, Ni/CeO_2 presents the lowest specific surface area (33 $m^2\ g^{-1}$) which increases as a function of the neodymium content, being the Ni/$Ce_{0.8}Nd_{0.2}O_{2-\delta}$ sample the one with the highest value (41 $m^2\ g^{-1}$). As-prepared catalysts were also characterized through EDS analysis to determine the total metal content and atomic percentage of nickel, results are compiled in Table 4. In all cases, the total metal content was slightly lower but close enough to the target nominal one (5 wt%).

Fig. 8 shows the backscattering SEM images of catalysts; the porosity observed in the Nd-doped ceria supports (Fig. 4) has been modified after nickel impregnation. This result correlates well with the N_2 adsorption–desorption experiments where a 2-fold decrease in the total pore volume is observed, corroborating that NiO particles affect the original mesoporous structure of the Nd-doped supports.

3.2.3 Ni catalysts reduction properties. After the structural and microstructural characterization, the catalysts reduction properties were studied through H_2-TPR experiments. The reduction profiles of calcined nickel catalysts are shown in Fig. 9, where hydrogen consumption is observed mostly in the 150–500 °C range. Different regions are identified in the TPR profiles, below and above 300 °C, labeled as α, β, and γ. The first region (α) has been related to the reduction of adsorbed reactive oxygen species coming from the formation of a surface Ni–O–Ce solid-solution by the incorporation of Ni ions into the CeO_2 crystal structure.[40,41] As Rietveld analysis showed, after Ni impregnation, a trend slightly increasing the lattice parameter of ceria is observed, indicating that the metal is somehow disturbing the crystal structure of the support. In this frame, the evolution of α peaks as a function of the Nd concentration shows a shift to higher temperatures accompanied by an intensity decrease, as clearly observed for the peak around 270 °C. Thus, it seems that the presence of Nd modifies the reduction properties of such species in ceria.

On the other hand, contributions above 300 °C, β and γ, have been assigned to the reduction of NiO particles with different degrees of interaction with the support.[40,41] The first, noted as β (*i.e.*, the shoulder observed at 316 and 322 °C, in Ni/CeO_2 and Ni/$Ce_{0.95}Nd_{0.05}O_{2-\delta}$ samples, respectively), is related to the reduction of Ni^{2+} to metallic Ni particles in low metal-support

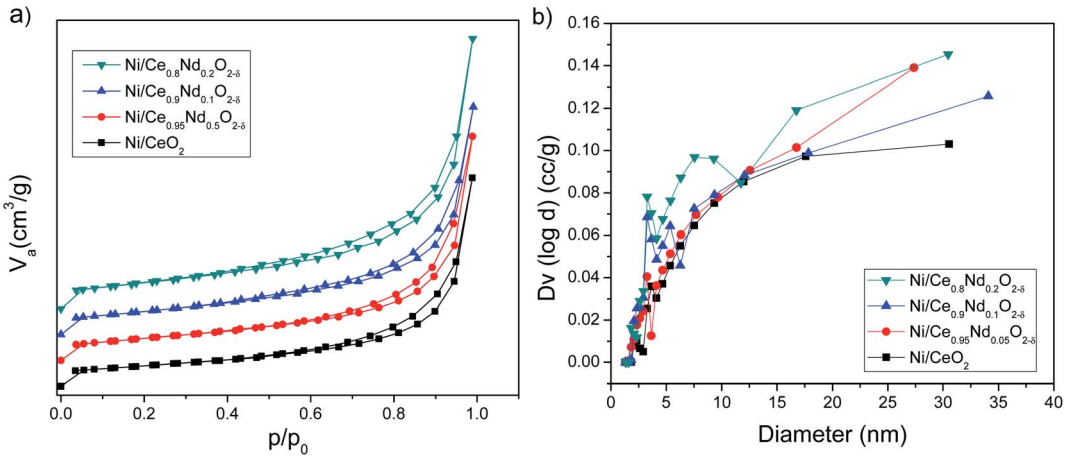

Fig. 7 N_2 adsorption–desorption isotherms of as-prepared Ni/ceria and Ni/Nd–ceria catalysts.

Open Access Article. Published on 07 September 2020. Downloaded on 1/24/2025 5:26:30 AM.
This article is licensed under a Creative Commons Attribution-NonCommercial 3.0 Unported Licence.

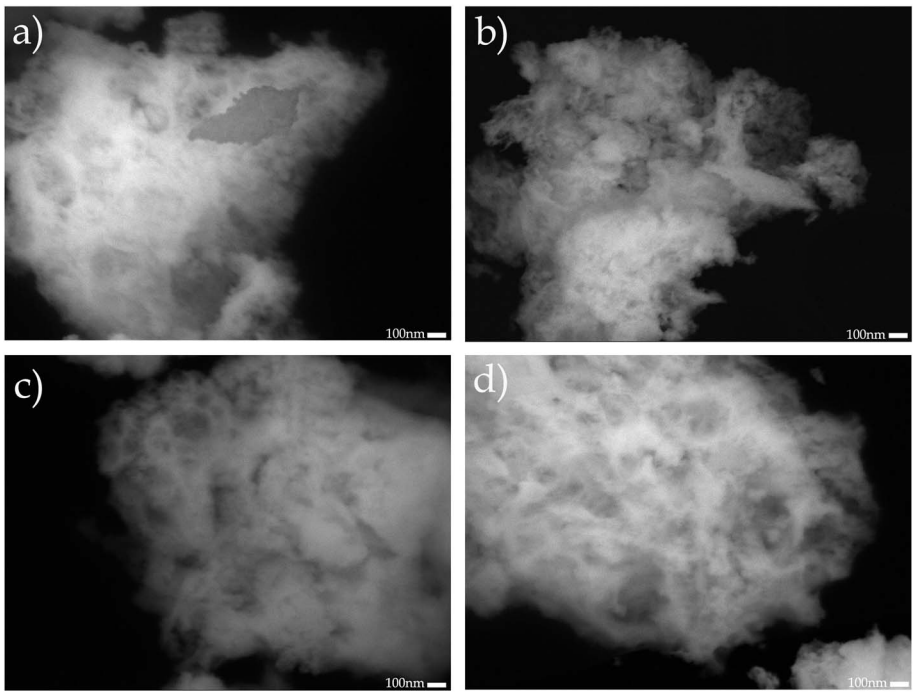

Fig. 8 Backscattering SEM images of the catalysts: (a) Ni/CeO_2, (b) $Ni/Ce_{0.95}Nd_{0.05}O_{2-\delta}$, (c) $Ni/Ce_{0.9}Nd_{0.1}O_{2-\delta}$, and (d) $Ni/Ce_{0.8}Nd_{0.2}O_{2-\delta}$.

interaction. The other one, identified as γ, with maxima at 356 and 359 °C, respectively, is associated with the reduction of NiO particles in stronger interaction with the support. It is evident that the reduction temperature of both contributions increases as a function of neodymium content, which means that the interaction between NiO particles and the support becomes stronger, as reported elsewhere.[8,12,41,42] Moreover, the better interaction between the nickel particles and Nd-doped ceria supports could be associated with an anchoring effect inside the mesoporous structure of the support, as revealed by the textural characterization results. It has been demonstrated that metal nanoparticles confined in mesoporous CeO_2 enhance the metal-support interaction and, therefore, the catalytic activity.[43]

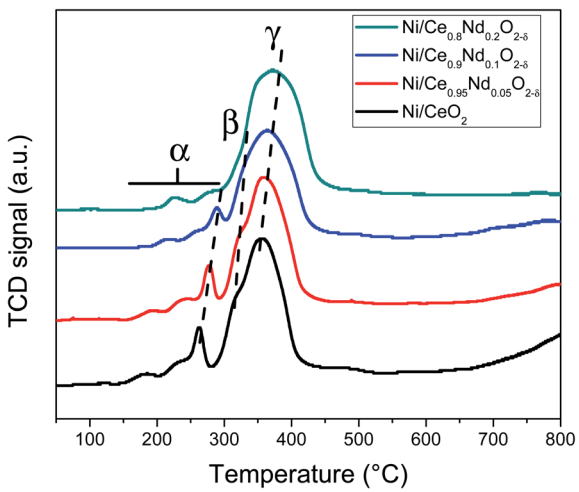

Fig. 9 H_2-TPR profiles of calcined nickel supported on ceria and Nd-doped ceria catalysts.

Specifically, a stronger Ni–CeO_2 interaction inhibits the Ni particles agglomeration and the coke deposition, which leads to better stability of the catalysts in the DRM reaction.[44]

3.3 Catalytic performance in the DRM reaction

3.3.1 Activity tests. Finally, the catalytic activity of *in situ* reduced Ni-supported materials was evaluated in the dry reforming of methane reaction (DRM). The reaction was studied in the temperature range of 600–800 °C at stoichiometric conditions of reactants and constant mass of catalyst. Fig. 10 shows the activity in terms of methane conversion (Fig. 10(a)) and carbon dioxide conversion (Fig. 10(b)), while the selectivity is presented as the H_2/CO molar ratio (Fig. 10(c)). Results indicate that CH_4 and CO_2 conversion increases almost linearly as a function of the temperature, and that nickel supported on pristine ceria is considerably less active than all the Ni/Nd–ceria catalysts. Table S1† shows the CH_4 and CO_2 conversion values displayed by all catalysts as a function of temperature. The CO_2 conversion in the Ni/CeO_2 catalyst is considerably higher than CH_4 in the whole temperature range. On the other hand, all Ni/Nd–ceria catalysts presented a similar behavior below 700 °C; above this temperature, both CH_4 and CO_2 conversion are almost equal. It has been reported that the activation energy is considerably higher for CH_4 than CO_2, indicating that activation of CH_4 is more temperature-sensitive than that of CO_2.[9] Thus, the reaction of methane becomes important as temperature increases. On the other hand, it has been reported for low-surface-area ceria and 10 mol% Gd-doped ceria that dissociation of methane proceeds almost exclusively *via* surface oxygen vacancies;[45] therefore, the oxygen vacancies generated by the introduction of Nd seems to enhance the activation of CH_4 and

 This journal is © The Royal Society of Chemistry 2020

Open Access Article. Published on 07 September 2020. Downloaded on 1/24/2025 5:26:30 AM.
This article is licensed under a Creative Commons Attribution-NonCommercial 3.0 Unported Licence.

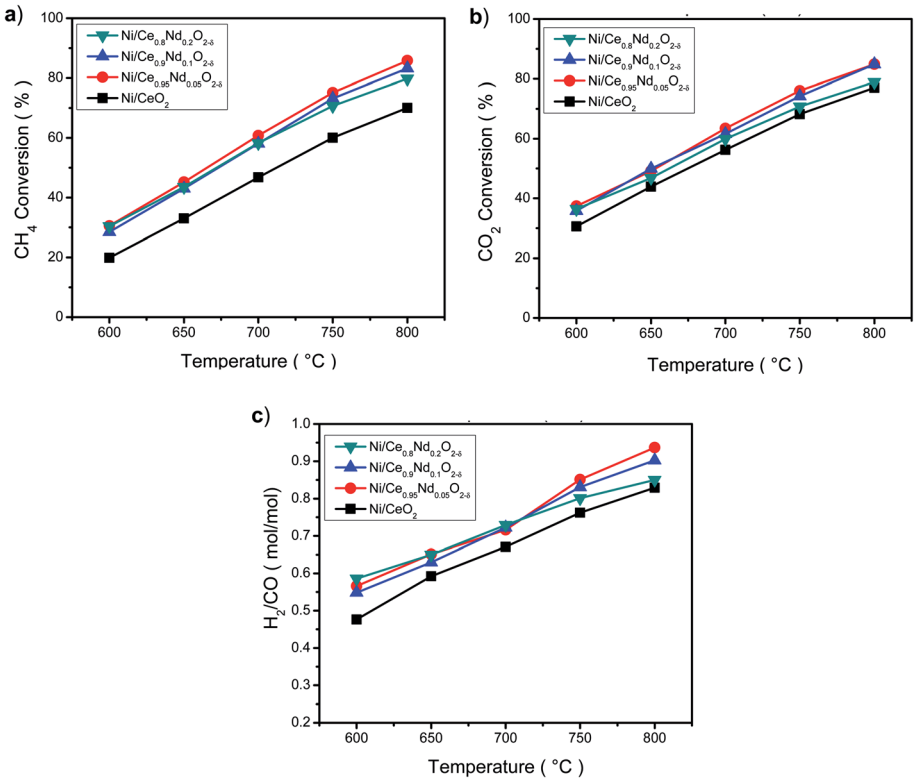

Fig. 10 Dry reforming of methane over *in situ* reduced nickel catalysts as a function of reaction temperature. (a) Methane conversion, (b) carbon dioxide conversion and (c) H_2/CO mole ratio. Reaction conditions: CH_4 : CO_2 molar ratio = 1, total flow 100 mL min^{-1}, GHSV = 48 000 h^{-1}.

should be responsible for its higher conversion compared to Ni/CeO_2.

One feature is observed; there is no linear dependence with the number of oxygen vacancies promoted by Nd, as the higher conversion was obtained with the Ni/$Ce_{0.95}Nd_{0.05}O_{2-\delta}$ catalyst. Looking closer to the Nd-doped ceria catalysts, Fig. 10 and Table S1,† the conversion of reactants at low temperatures does not vary considerably. At the same time, above 700 °C, some differences appear, notably a decrease in the conversion as neodymium content increases, mostly in Ni/$Ce_{0.8}Nd_{0.2}O_{2-\delta}$ catalyst. At high temperatures, low-content Nd samples perform better in DRM reaction.

On the other hand, as the conversion of reactants increases with the temperature, the H_2/CO molar ratio (Fig. 10(c)) also increases, and all the Nd-doped catalysts show a better selectivity towards H_2, compared to the Ni/CeO_2 catalyst. According to the stoichiometry of DRM reaction (eqn (1)), the maximum value of the H_2/CO molar ratio is 1. This ratio increases as temperature rises, indicating that the DRM reaction is favored at high temperatures, however, other side reactions could be taking place. A value lower than 1 for the H_2/CO molar ratio probably indicates the RWGS reaction (eqn (4)) occurs as CO is produced in detriment of H_2, and more CO_2 is converted.[13]

$$H_2 + CO_2 \leftrightarrow H_2O + CO, \quad \Delta H = +41 \text{ kJ mol}^{-1} \tag{4}$$

In the range of 650–1000 °C, RWGS is the main side reaction, and other reactions as CH_4 decomposition (eqn (5)) and the Boudouard reaction (eqn (6)), leading to carbon residues, also could take place.[46,47]

$$CH_4 \leftrightarrow C + 2H_2, \quad \Delta H = +74.9 \text{ kJ mol}^{-1} \tag{5}$$

$$2CO \leftrightarrow CO_2 + C, \quad \Delta H = -172 \text{ kJ mol}^{-1} \tag{6}$$

The behavior of the H_2/CO molar ratio as a function of temperature indicates that the RWGS reaction is taking place, but reverse Boudouard reaction may be also a source of CO at high temperature. In the high-temperature regime, as the content of Nd decreases, the H_2/CO ratio improves. The highest value found among samples was 0.95 at 800 °C displayed by Ni/$Ce_{0.95}Nd_{0.05}O_{2-\delta}$ catalyst.

Nevertheless, despite the enhanced properties as higher SSA, smaller crystallite size, and higher amount of oxygen vacancies achieved as Nd concentration increases in the support, the catalytic properties do not show significant differences.

Overall, it must be pointed out that Nd-doped ceria improves the selectivity towards hydrogen of the nickel-based catalyst in the dry reforming of methane reaction. This result correlates well with the overall activity behavior of samples.

3.3.3 Stability tests. The catalytic stability of *in situ* reduced catalysts was studied at 700 °C during 24 h at constant mass of catalyst. Fig. 11 shows the CH_4 (a), and CO_2 (b) conversions, as well as the H_2/CO molar ratio (c). Table S2† shows the conversion values as a function of time on-stream and the % difference between initial and final reactants conversion. These results confirm the better performance of Ni/Nd–ceria catalysts

Open Access Article. Published on 07 September 2020. Downloaded on 1/24/2025 5:26:30 AM.
This article is licensed under a Creative Commons Attribution-NonCommercial 3.0 Unported Licence.

compared to Ni/CeO_2 catalyst; the latter undergoes important deactivation throughout the 24 h catalytic run. The difference between the initial and final conversion of methane after 24 h on-stream at 700 °C (Table S2†) is 38%; the CO_2 conversion follows the same trend.

On its side, all the Nd-doped catalysts present similar behavior, although some differences are observed. In general, the CH_4 and CO_2 conversions drop only about 10% after 24 h reaction. In comparison, the decay in the conversion of reactants after 24 h on-stream at 700 °C is about three times larger in the undoped ceria catalyst. Therefore, the addition of Nd enhances the stability of the catalysts.

The trend of H_2/CO molar ratio as a function of time on-stream (Fig. 11(c)) follows that of conversion of reactants, however, it is worth noting that the selectivity towards hydrogen in the 24 h run is higher in the Nd-doped catalysts compared to the Ni/CeO_2 sample.

Deposition of carbon residues on the surface of the catalyst, blocking the active sites, is one of the deactivation mechanisms in DRM reaction, so it is relevant to know the nature of such deposits in this case.

3.4 Characterization of spent catalysts: carbon deposition analysis by O_2-TPO

O_2-TPO experiments were performed after the stability tests (700 °C/24 h) to assess the amount and type of carbon deposits on the surface of spent catalysts, Fig. 12. These experiments help to show the impact of neodymium to reduce coke deposition and, therefore, the enhancement of stability of catalysts. In all cases, O_2-TPO profiles are composed of several contributions (as evidenced by the deconvolution). In general, three types of carbon deposits are found in DRM spent catalysts:[13] (i) below 400 °C related to hydrocarburic carbon, (ii) between 400–700 °C assigned to amorphous carbon and (iii) above 700 °C corresponding to graphitic carbon. All samples present a tiny

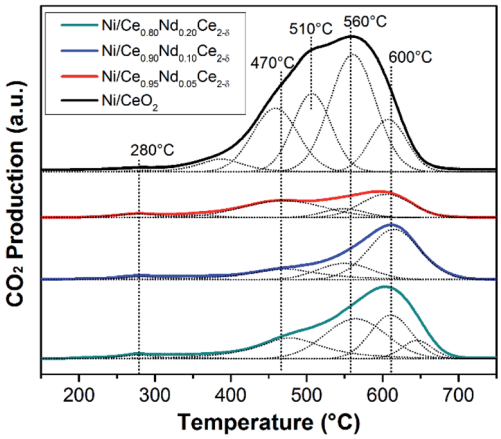

Fig. 12 O_2-TPO profiles of spent nickel-based catalysts.

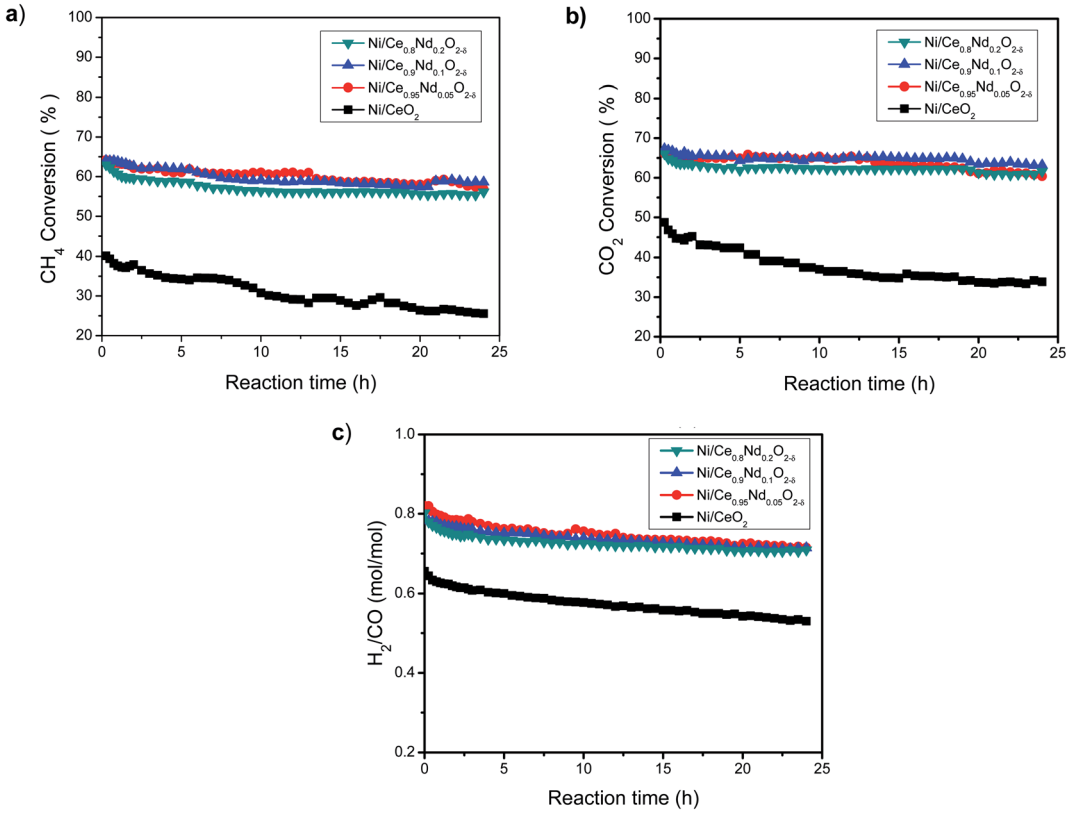

Fig. 11 Dry reforming of methane over *in situ* reduced nickel catalysts as a function of time on-stream. (a) Methane conversion, (b) carbon dioxide conversion and (c) H_2/CO mole ratio. Reaction conditions: reaction temperature = 700 °C; $CH_4 : CO_2$ molar ratio = 1, total flow 100 mL min^{-1}, GHSV = 48 000 h^{-1}.

Open Access Article. Published on 07 September 2020. Downloaded on 1/24/2025 5:26:30 AM.
This article is licensed under a Creative Commons Attribution-NonCommercial 3.0 Unported Licence.

contribution at 280 °C (hydrocarburic carbon), whereas no peaks above 700 °C are observed; then most of the CO_2 production comes from the gasification of amorphous carbon and analysis focus on this zone.

As observed, the undoped catalyst (Ni/CeO_2) presents the highest CO_2 production, composed by four contributions at different temperatures related to carbon deposits interacting with the different surface species. The amount of the deposited carbon displayed as gasified CO_2 in Table 5, is 4, 3, and 2 times larger in Ni/CeO_2 catalyst compared to $Ni/Ce_{0.95}Nd_{0.05}O_{2-\delta}$, $Ni/Ce_{0.9}Nd_{0.1}O_{2-\delta}$, and $Ni/Ce_{0.8}Nd_{0.2}O_{2-\delta}$, respectively. From these results, the lower stability of Ni supported on undoped CeO_2 is related, at least in part, to the higher amount of carbon deposits.

On the other hand, the O_2-TPO profiles of the spent Nd-doped catalysts are composed by three clear contributions already observed in the undoped catalyst, around 470, 560 and 600 °C. From Table 5, the $Ni/Ce_{0.95}Nd_{0.05}O_{2-\delta}$ sample shows the lowest CO_2 production, and as the content of neodymium increases, the carbon dioxide production follows. The lower amount of carbon deposits in the $Ni/Ce_{0.95}Nd_{0.05}O_{2-\delta}$ catalyst correlates well with its improved activity. Under DRM reaction conditions, the oxygen vacancies in ceria have been related to a better CO_2 activation and carbon gasification at the metal-support interfaces, with the following mechanism: CO_2 is chemisorbed over the support and decomposes into CO, which is released, while the oxygen atom fills one oxygen vacancy. Finally, the formed oxygen atom oxidizes the carbon deposit to CO/CO_2, avoiding its accumulation on the metal site.[39]

A high number of oxygen vacancies is expected to have a positive impact on controlling the carbon deposits on the surface of the catalysts. This situation is occurring in the $Ni/Ce_{0.95}Nd_{0.05}O_{2-\delta}$ sample, as the amount of deposited carbon measured as gasified CO_2 is 4 times lower than in Ni/CeO_2; however, as Nd concentration increases and so does the number of oxygen vacancies in the support, the beneficial input of this property is not observed, as higher amounts of carbon remain at the surface of the catalysts. In other words, the increase in the Nd doping of the support is not reflected in a significant improvement in the anti-coking properties of the catalyst or in the activity, as previously shown. However, it is important to remark that despite this, Ni/Nd–ceria are more stable and active than Ni/CeO_2, as shown for 24 h runs on-stream (Fig. 11).

Besides the remarkable redox properties of ceria and doped ceria materials, connected with oxygen mobility, the acid–base properties of the surface play an important role on the catalytic performance for many reactions. Addition of rare-earth dopants in ceria and ceria-based supports change the acid/base properties of the surface.[48–51] Recently, it was reported[48] that by doping CeO_2 and CeO_2/ZrO_2 solid solution with Nd, the basicity of the supports is reduced.

It is well known that the role of basic sites in the dry reforming reaction is to enhance the activation of acidic CO_2 on the support surface and to inhibit carbon deposition on the catalyst.[52] As shown in Table S1,† CO_2 conversion by Nd-doped catalysts decreases as a function of Nd content, which is in a good agreement with the loss of basicity and, therefore, diminishing the gasification capacity of the carbon residues on the surface issued from methane dehydrogenation. An optimum Nd concentration would lead to the right balance between redox and acid/base properties as the key factor to get active and stable catalysts for DRM reaction.

Further research in this regard is necessary to better understand the roles of both properties.

Table 5 Quantitative analysis of O_2-TPO profiles of spent catalysts

Catalyst	CO_2 production (μmol)
Ni/CeO_2	0.436
$Ni/Ce_{0.95}Nd_{0.05}O_{2-\delta}$	0.101
$Ni/Ce_{0.9}Nd_{0.1}O_{2-\delta}$	0.140
$Ni/Ce_{0.8}Nd_{0.2}O_{2-\delta}$	0.209

4. Conclusions

Nickel (5 wt%) supported on $Ce_{1-x}Nd_xO_{2-\delta}$ ($x = 0$, 0.05, 0.1 and 0.2) was studied in the DRM reaction. Nd-doped ceria supports were synthesized by the EDTA–citrate complexing method. It was proved by XRD (Rietveld refinement) and Raman spectroscopy analysis (Raman shift in the main F_{2g} band) that all Nd was incorporated into the ceria crystal structure, leading to a linear increase of oxygen vacancies as a function of Nd content. Also, doped supports showed a developed mesoporous structure, higher specific surface area, and smaller crystallite size, compared to undoped ceria. All the Ni/Nd–ceria catalysts were more active and stable in the DRM reaction than the Ni/CeO_2 catalyst, indicating the beneficial impact of Nd incorporation. However, the amount of deposited carbon in spent Nd-doped catalysts increases as a function of the dopant concentration, despite the enhanced number of oxygen vacancies present. Nd doping in ceria leads to a change of the acid/base properties of the support diminishing the gasification capacity of the carbon residues issued from methane dehydrogenation. An adequate balance between redox and acid/base properties directly related to the Nd concentration, is needed to fully develop the enhanced catalytic properties of Ni/Nd–ceria catalysts in DRM reaction.

Conflicts of interest

There are not conflicts to declare.

Acknowledgements

A. Morales for XRD diffraction patterns, C. Zorrilla for Raman spectra and M. Aguilar-Franco for EDS measurements. Daniel G. Araiza and Melissa Méndez-Galván thank the scholarship financial support of PNPC-CONACyT.

References

1 S. Arora and R. Prasad, *RSC Adv.*, 2016, **6**, 108668–108688.

Open Access Article. Published on 07 September 2020. Downloaded on 1/24/2025 5:26:30 AM.
This article is licensed under a Creative Commons Attribution-NonCommercial 3.0 Unported Licence.

2 S. Zaman and K. J. Smith, *Catal. Rev.: Sci. Eng.*, 2012, **54**, 41–132.
3 A. Abdulrasheed, A. A. Jalil, Y. Gambo, M. Ibrahim, H. U. Hambali and M. Y. Shahul Hamid, *Renewable Sustainable Energy Rev.*, 2019, **108**, 175–193.
4 G. Zhang, J. Liu, Y. Xu and Y. Sun, *Int. J. Hydrogen Energy*, 2018, **43**, 15030–15054.
5 B. Abdullah, N. A. Abd Ghani and D. V. N. Vo, *J. Cleaner Prod.*, 2017, **162**, 170–185.
6 S. Bhavsar and G. Veser, *Energy Fuels*, 2013, **27**, 2073–2084.
7 P. Kumar, Y. Sun and R. O. Idem, *Energy Fuels*, 2007, **21**, 3113–3123.
8 N. Wang, W. Qian, W. Chu and F. Wei, *Catal. Sci. Technol.*, 2016, **6**, 3594–3605.
9 L. Pino, C. Italiano, M. Laganà, A. Vita and V. Recupero, *Catal. Sci. Technol.*, 2020, **10**, 2652–2662.
10 H. R. Gurav, S. Dama, V. Samuel and S. Chilukuri, *J. CO2 Util.*, 2017, **20**, 357–367.
11 Z. Bian, S. Das, M. H. Wai, P. Hongmanorom and S. Kawi, *ChemPhysChem*, 2017, **18**, 3117–3134.
12 X. Du, D. Zhang, L. Shi, R. Gao and J. Zhang, *J. Phys. Chem. C*, 2012, **116**, 10009–10016.
13 D. G. Araiza, D. G. Arcos, A. Gómez-Cortés and G. Díaz, *Catal. Today*, 2019, DOI: 10.1016/j.cattod.2019.06.018.
14 A. Romero-Núñez and G. Díaz, *RSC Adv.*, 2015, **5**, 54571–54579.
15 E. W. McFarland and H. Metiu, *Chem. Rev.*, 2013, **113**, 4391–4427.
16 P. Sudarsanam, K. Kuntaiah and B. M. Reddy, *New J. Chem.*, 2014, **38**, 5991–6001.
17 D. N. Durgasri, T. Vinodkumar, F. Lin, I. Alxneit and B. M. Reddy, *Appl. Surf. Sci.*, 2014, **314**, 592–598.
18 M. Biswas and S. Bandyopadhyay, *Metall. Mater. Trans. A*, 2013, **44**, 5251–5258.
19 S. S. Patil, H. P. Dasari and H. Dasari, *Nano-Struct. Nano-Objects*, 2019, **20**, 100388.
20 J. Zhang, C. Ke, H. Wu, J. Yu and J. Wang, *J. Solid State Chem.*, 2016, **243**, 57–61.
21 S. V. Chavan, P. U. M. Sastry and A. K. Tyagi, *J. Alloys Compd.*, 2008, **456**, 51–56.
22 W. C. Wu, J. T. Huang and A. Chiba, *J. Power Sources*, 2010, **195**, 5868–5874.
23 H. Liu, Y. Li, H. Wu, W. Yang and D. He, *Chin. J. Catal.*, 2014, **35**, 1520–1528.
24 X. Fang, J. Zhang, J. Liu, C. Wang, Q. Huang, X. Xu, H. Peng, W. Liu, X. Wang and W. Zhou, *J. CO2 Util.*, 2018, **25**, 242–253.
25 D. G. Araiza, A. Gómez-Cortés and G. Díaz, *Catal. Today*, 2017, **282**, 185–194.
26 N. Doebelin and R. Kleeberg, *J. Appl. Crystallogr.*, 2015, **48**, 1573–1580.
27 R. Aadhavan and K. S. Babu, *RSC Adv.*, 2015, **5**, 83538–83545.
28 S. C. Rood, H. B. Ahmet, A. Gomez-Ramon, L. Torrente-Murciano, T. R. Reina and S. Eslava, *Appl. Catal., B*, 2019, **242**, 358–368.
29 A. Singhania and A. N. Bhaskarwar, *Int. J. Hydrogen Energy*, 2018, **43**, 4818–4825.
30 D. He, H. Hao, D. Chen, J. Liu, J. Yu, J. Lu, F. Liu, G. Wan, S. He and Y. Luo, *Catal. Today*, 2017, **281**, 559–565.
31 Y. Lee, G. He, A. J. Akey, R. Si, M. Flytzani-Stephanopoulos and I. P. Herman, *J. Am. Chem. Soc.*, 2011, **133**, 12952–12955.
32 S. Lowell, J. E. Shields, M. A. Thomas and M. Thommes, *Characterization of Porous Solids and Powders: Surface Area, Pore Size and Density, Particle Technology Series*, Kluwer Academic Publishers, London, 2004.
33 X. Zheng, Y. Li, L. Zhang, L. Shen, Y. Xiao, Y. Zhang, C. Au and L. Jiang, *Appl. Catal., B*, 2019, **252**, 98–110.
34 J. Wang, Q. Ma, Y. Wang, Z. Li, Z. Li and Q. Yuan, *Chem. Soc. Rev.*, 2018, **47**, 8766–8803.
35 L. Katta, P. Sudarsanam, G. Thrimurthulu and B. M. Reddy, *Appl. Catal., B*, 2010, **101**, 101–108.
36 A. Singhania, *Ind. Eng. Chem. Res.*, 2017, **56**, 13594–13601.
37 T. Odedairo, J. Chen and Z. Zhu, *Catal. Commun.*, 2013, **31**, 25–31.
38 P. H. Tu, D. N. Le, T. D. Dao, Q. Tran, T. C. D. Doan, Y. Shiratori and C. M. Dang, *Int. J. Hydrogen Energy*, 2020, **45**, 18363–18375.
39 I. Luisetto, S. Tuti, C. Romano, M. Boaro, E. Di Bartolomeo, J. K. Kesavan, S. S. Kumar and K. Selvakumar, *J. CO2 Util.*, 2019, **30**, 63–78.
40 W. Shan, M. Luo, P. Ying, W. Shen and C. Li, *Appl. Catal., A*, 2003, **246**, 1–9.
41 Z. Xiao, Y. Li, F. Hou, C. Wu, L. Pan, J. Zou, L. Wang, X. Zhang, G. Liu and G. Li, *Appl. Catal., B*, 2019, **258**, 117940.
42 Z. Xiao, X. Zhang, F. Hou, C. Wu, L. Wang and G. Li, *Appl. Surf. Sci.*, 2020, **503**, 144319.
43 M. Mao, H. Lv, Y. Li, Y. Yang, M. Zeng, N. Li and X. Zhao, *ACS Catal.*, 2016, **6**, 418–427.
44 M. Li and A. C. van Veen, *Appl. Catal., B*, 2018, **237**, 641–648.
45 K. J. Warren and J. R. Scheffe, *J. Phys. Chem. C*, 2019, **123**, 13208–13218.
46 W. J. Jang, D. W. Jeong, J. O. Shim, H. M. Kim, H. S. Roh, I. H. Son and S. J. Lee, *Appl. Energy*, 2016, **173**, 80–91.
47 J. M. Lavoie, *Front. Chem.*, 2014, **2**, 1–17.
48 A. Pappacena, R. Razzaq, C. de Leitenburg, M. Boaro and A. Trovarelli, *Inorganics*, 2018, **6**, 1–15.
49 Q. Jin, Y. Shen and S. Zhu, *Chin. J. Chem.*, 2016, **34**, 1283–1290.
50 Q. Jin, Y. Shen, S. Zhu, H. Li and Y. Li, *J. Mater. Res.*, 2017, **32**, 2438–2445.
51 D. Stoian, F. Medina and A. Urakawa, *ACS Catal.*, 2018, **8**, 3181–3193.
52 M. A. A. Aziz, A. A. Jalil, S. Wongsakulphasatch and D. N. Vo, *Catal. Sci. Technol.*, 2020, **10**, 35–45.

 This journal is © The Royal Society of Chemistry 2020